Research Article Vol. 31, No. 3 / 30 Jan 2023 / Optics Express 4140
Optics EXPRESS

Broadband integrated polarization splitter and rotator using subwavelength grating claddings

MD BORHAN MIA,[1] NAFIZ JAIDYE,[2] ISHTIAQUE AHMED,[2] SYED Z. AHMED,[1] AND SANGSIK KIM[1,2,3,*]

[1]Department of Electrical and Computer Engineering, Texas Tech University, Lubbock, Texas 79409, USA
[2]Department of Physics and Astronomy, Texas Tech University, Lubbock, Texas 79409, USA
[3]School of Electrical Engineering, Korea Advanced Institute of Science and Technology, Daejeon 34141, Republic of Korea
[*]sangsik.kim@kaist.ac.kr

Abstract: We present a broadband integrated photonic polarization splitter and rotator (PSR) using adiabatically tapered coupled waveguides with subwavelength grating (SWG) claddings. The PSR adiabatically rotates and splits the fundamental transverse-magnetic (TM_0) input to the fundamental transverse-electric (TE_0) mode in the coupler waveguide, while passing the TE_0 input through the same waveguide. The SWGs work as an anisotropic metamaterial and facilitate modal conversions, making the PSR efficient and broadband. We rigorously present our design approaches in each section and show the SWG effect by comparing with and without the SWG claddings. The coupling coefficients in each segment explicitly show a stronger coupling effect when the SWGs are included, confirmed by the coupled-mode theory simulations. The full numerical simulation shows that the SWG-PSR operates at 1500–1750 nm (≈250 nm) wavelengths with an extinction ratio larger than 20 dB, confirmed by the experiment for the 1490–1590 nm range. The insertion losses are below 1.3 dB. Since our PSR is designed based on adiabatical mode evolution, the proposed PSR is expected to be tolerant to fabrication variations and should be broadly applicable to polarization management in photonic integrated circuits.

1. Introduction

Silicon (Si) photonics on a silicon-on-insulator (SOI) wafer is a promising photonic integrated circuit (PIC) platform, with its compatibility with the well-established complementary metal-oxide-semiconductor (CMOS) process. The large index contrast between silicon and oxide cladding confines telecommunication light at hundreds of nanometers, allowing a compact circuit footprint with multiple functionalities. The waveguide asymmetry in height and width leads to a birefringence, resulting in polarization-dependent transverse-electric (TE) and transverse-magnetic (TM) modes. To fully utilize the polarizations in a PIC, polarization controlling components such as polarization beam splitter (PBS) [1–7], polarization rotator [8–11], and polarization splitter-rotator (PSR) [12–30] are required to be integrated on a chip. The PSR is a component that splits TE and TM inputs into two separate paths and then rotates one polarization to the other orthogonal one while keeping the other polarization status the same (usually, it rotates TM input to TE, while keeping TE input to TE). In this way, polarization status inside the circuit can be consistent regardless of input polarization. The mixed polarization input will also be separated into two different paths, sorting out the polarization status. Thus, PSRs play a significant role in the polarization-transparent PICs [31–33], polarization-entangled photons [34,35], coherent optical transceivers [36,37], and on-chip optical communications [38].

A PSR is essentially composed of two modal conversions, i.e., polarization split and rotation. Two mechanisms, i.e., mode-coupling and mode-evolution, can be utilized for manipulating waveguide modes, and PSRs were designed with either mode-coupling [12–17], mode-evolution [18–27], or hybrid (that uses both mode-coupling and mode-evolution) [28–30] approaches.

#479195 https://doi.org/10.1364/OE.479195
Journal © 2023 Received 27 Oct 2022; revised 15 Dec 2022; accepted 3 Jan 2023; published 20 Jan 2023

Optics EXPRESS

Mode-coupling is based on matching the modal phases; thus, it generally exhibits a relatively short device length but high sensitivity to fabrication imperfections and limited bandwidth. In contrast, mode-evolution works by gradual change in the modal index, reducing the geometric sensitivity that allows tolerance to fabrication errors and broader bandwidth in the trade of a longer device length.

Recently, subwavelength grating (SWG) metamaterials have been used to enhance the performances of many Si photonic devices, providing additional degrees of freedom to engineer modal properties [39–44]. SWGs work as a homogenized anisotropic medium whose effective index and anisotropy can be engineered by changing the filling fraction and tilting angle [45,46]. Using these modal engineering capabilities, SWGs have been used to reduce the skin depth and manipulate the dielectric perturbation of guided modes for lower crosstalk [47–49] and engineering the birefringence to design various PBSs [2–7]. For example, a notably high extinction ratio >50 dB PBS was demonstrated with an extreme suppression of waveguide crosstalk [5], and an ultra-broadband PBS having a bandwidth >200 nm was demonstrated with SWGs [2–4].

In this paper, we present a broadband PSR design with SWG metamaterials. The PSR is designed to rotate the TM input to TE, then split it into a coupled waveguide while keeping the TE input in the same waveguide without rotation. Both modal conversion sections, i.e., rotation and splitting, are designed based on adiabatic evolution by tapering the waveguide cores, providing broadband and fabrication tolerance to our device. Compared to conventional strip-based designs, the SWGs enhance coupling strengths, leading to highly efficient modal conversions with shorter device lengths and broader bandwidth. In the following, we present our design and optimization processes, compare them with a conventional strip design, and numerically and experimentally demonstrate the broadband SWG-based PSR on an SOI platform.

2. Schematics and design

2.1. Schematics of the polarization rotator and splitter

The proposed PSR is designed on a 220 nm thick SOI platform. Figure 1(a) illustrates the schematic of the PSR, which consists of two modal conversion sections: mode rotation and mode splitting. The PSR has one input and two output ports; the TE_0 and TM_0 inputs are routed to waveguide-A (red trace) and waveguide-B (yellow trace), respectively. In the mode rotation section, waveguide-A is tapered as w_A=450–700 nm along the taper length L_{t1} for the modal transition from the TM_0 to the TE_1. In the following mode splitting section, a coupled waveguide-B is introduced and linearly tapered as w_B=150–500 nm along the taper length L_{t2} while keeping the width of waveguide-A the same as w_A=700 nm. With this, the TE_1 mode in waveguide-A can smoothly couple to the TE_0 mode in waveguide-B. Due to a large phase mismatch with other modes, the TE_0 input will not be converted/coupled throughout the entire sections and will pass to the waveguide-A output. The gap between two waveguides is set to $g=w_{swg}+2g_{off}$=350 nm, where w_{swg}=250 nm and g_{off}=50 nm. The periodicity and the filling fraction of SWGs are set to Λ=100 nm and ρ=0.5, respectively. The air serves as a cladding to break the vertical symmetry and achieve efficient polarization conversion [50,51]. The yellow arrow in Fig. 1(a) represents the guided path of the TM_0 input toward the TE_0 output, and Fig. 1(b) shows the corresponding field profiles in each modal transition (i.e., $TM_{0A} \rightarrow TE_{1A} \rightarrow TE_{0B}$). Due to a strong modal overlap, the injected TM_0 mode is converted to the TE_1 transitional mode, and then it adiabatically couples to the TE_0 mode in the waveguide-B output. The red arrow in Fig. 1(a) indicates this guided path of TE_0 mode, and Fig. 1(c) shows the corresponding mode field profiles. For the TE_0 input, it neither converts nor couples to other modes and passes through the output waveguide-A. S-bends are added at the output ports to smoothly transit from SWG to strip waveguides. In the following sections, we will present the design and optimization of each section in detail and compare our SWG-PSR with conventional strip-PSR.

Optics EXPRESS

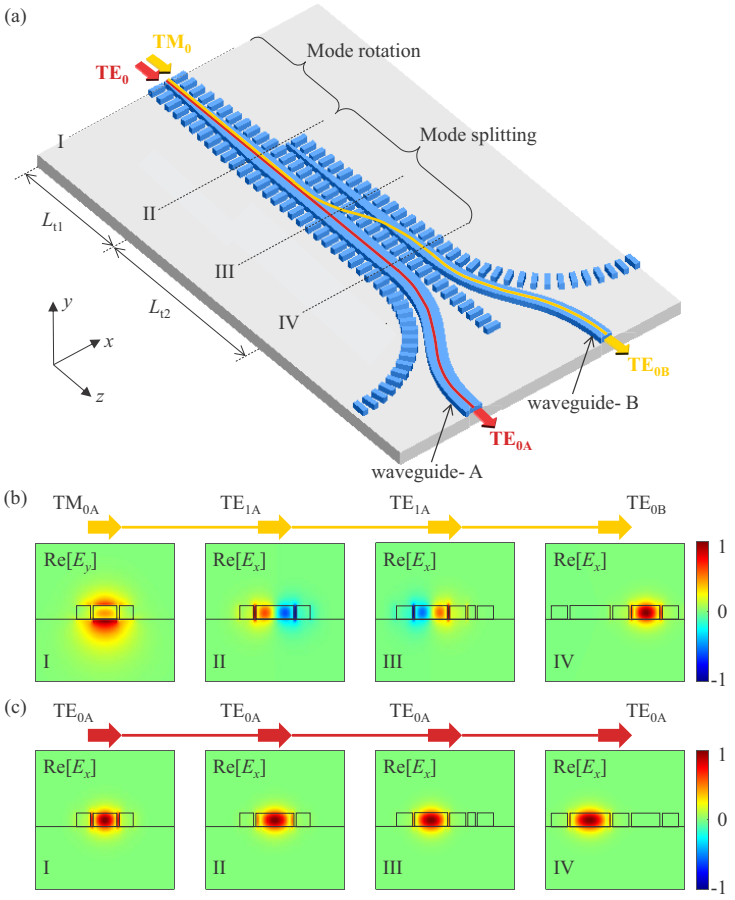

Fig. 1. (a) The schematic of the proposed polarization splitter and rotator (PSR) with subwavelength gratings (SWGs). Blue and grey represent Si and SiO_2, respectively. The PSR consists of two sections: mode rotation and mode splitting. Waveguide-A is tapered w_A=450–700 nm along the L_{t1}, followed by a constant width w_A=700 nm. Waveguide-B starts at the mode splitting section and is gradually tapered w_B=150–500 nm along the L_{t2}. The red and yellow arrows mark the paths of the TE_0 and TM_0 inputs, respectively. The mode profiles at each transition section: (b) TM_0 (yellow path) and (c) TE_0 (red path) inputs. The Si height, SWG period, and SWG filling fraction are set to h=220 nm, Λ=100 nm, and ρ=0.5, respectively.

2.2. *Mode rotation section*

First, the mode rotation section is designed to rotate the TM_0 to TE_1 while keeping the TE_0 input the same. The vertical asymmetry with an air cladding leads to a coupling between the TM_0 and TE_1, and the adiabatic tapering smoothly translates their modal conversion. This conversion can be optimized by engineering the taper width $w_A(z)$ and the taper length L_{t1}. Figure 2(a) shows the cross-sections of waveguide-A, with (left) and without (right) SWG claddings. The case of a strip waveguide without SWG claddings is shown here for comparison to examine the effect of SWG cladding. Note that SWG is modeled using the effective medium theory (EMT) with permittivities $\varepsilon_x = \varepsilon_y = \varepsilon_{\parallel}$ and $\varepsilon_z = \varepsilon_{\perp}$, which follow [52]:

$$\varepsilon_{\parallel} = \rho\varepsilon_{Si} + (1-\rho)\varepsilon_{Air} \tag{1a}$$

Optics EXPRESS

$$\varepsilon_{\perp} = \frac{\varepsilon_{\mathrm{Si}}\varepsilon_{\mathrm{Air}}}{\rho\varepsilon_{\mathrm{Air}} + (1-\rho)\varepsilon_{\mathrm{Si}}} \tag{1b}$$

where, $\varepsilon_{\mathrm{Si}}$ and $\varepsilon_{\mathrm{Air}}$ are the permittivities of silicon and air, respectively. The filling fraction is set to ρ=0.5. The width of SWGs and offset gap are fixed at w_{swg}=250 nm and g_{off}=50 nm, respectively. The offset g_{off} is introduced to avoid significant scattering from the sharp corner, reducing the insertion loss. Figure 2(b) plots the effective refractive indices n_{eff} of the guided modes in SWG-clad (solid lines) and strip (dashed lines) waveguides. Blue, orange, and yellow represent TE_0, $\mathrm{TM}_0 \rightarrow \mathrm{TE}_1$, and $\mathrm{TE}_1 \rightarrow \mathrm{TM}_0$ modal indices, respectively. Because the TE_0 has a considerably higher effective index than other modes, it passes through the tapered waveguide without coupling to other modes. However, for the TM_0 input, there is a mode hybridization near $w_{\mathrm{A}} \approx 650$ nm, translating TM_0 to TE_1 (following the trajectories of orange lines). The trajectories are chosen to have smooth modal transitions rather than abrupt change. Based on this, we taper the waveguide-A width as w_{A}=450–700 nm, fully covering the $\mathrm{TM}_0 \rightarrow \mathrm{TE}_1$ modal conversion. Here the insertion of SWGs will cause a stronger hybridization, which makes the modal transition more efficient, shortening the required conversion length. To compare the hybridization strength between SWG-clad and strip waveguides, we evaluated the local coupled-mode coefficients given by [53,54]:

$$\kappa_i = \frac{\omega\varepsilon_0}{4}\frac{1}{\beta_n - \beta_m}\iint \frac{\partial\varepsilon_i(x,y,z)}{\partial z}E_{ni}^{*}(x,y)\cdot E_{mi}(x,y)dxdy \tag{2}$$

where, the subscript i= x, y, and z and $\varepsilon(x,y,z)$ is the relative permittivity distribution of the waveguides. The E_m and E_n are the normalized electric field components of the local modes m and n, and the β_m and β_n are the corresponding propagation constants. The local perturbation described by $\partial\varepsilon(x,y,z)/\partial z$ is implemented by having discrete cross-sections with a 2 nm step size along the tapering direction. Figure 2(c) shows the numerically calculated $\kappa = \kappa_x + \kappa_y + \kappa_z$ of SWG-clad (solid) and strip (dashed) waveguides as a function of w_{A}. The κ_x, κ_y, and κ_z are coupling coefficients from each field components, collectively affecting the overall coupling coefficient κ. Note that the κ of the SWG is much higher than that of the strip, which will make the transition via SWG more efficient than the strip waveguide without SWG claddings.

To confirm the TM_0 to TE_1 modal rotation and their conversion efficiency (*CE*) per the taper length L_{t1}, we performed the eigenmode expansion (EME) simulations. We launched the TM_0 mode while linearly tapering the waveguide-A as w_{A}=450–700 nm. Figure 2(d) shows the top view of the EME simulation domain, and Fig. 2(e) plots the *CE* of SWG-clad (orange) and strip (blue) waveguides. The solid and dashed lines show the modal conversions of TM_0 to TE_1 and TM_0 to TM_0, respectively. The circles are the calculated results of the local coupled-mode theory using the κ from Fig. 2(c), further confirming our numerical approaches [53,54]. As the taper length increases, the *CE*s of the modal rotation approaches 100%, which is the notable characteristic of mode-evolution-based modal transition. Between SWG-clad and strip waveguides, as expected from Fig. 2(c), the SWG exhibits a shorter conversion length than the strip case (To achieve *CE* >99.50%, L_{t1}=40 μm is required for SWG and L_{t1}=65 μm for strip). This is due to the stronger coupling strength induced by the SWG-clad than the strip waveguide.

2.3. Mode splitting section

In the mode splitting section, a coupler waveguide-B is introduced to split the TE_1 mode, which was rotated from the TM_0 in the first section. An adiabatic tapering of the waveguide-B will allow the mode evolutionary transition from the TE_1 mode in the waveguide-A to the TE_0 mode in the waveguide-B while keeping the TE_0 input in the waveguide-A. To optimize this transition, we simulated the modal evolution by varying the w_{B} of the coupled waveguides schemes as in Fig. 3(a): SWG-clad (left) and strip (right). Figure 3(b) shows the simulated n_{eff} of the coupled SWG-clad (solid lines) and strip (dashed lines) waveguides as a function of w_{B} for the tapered widths as 150–500 nm. The width of waveguide-A is fixed to w_{A}=700 nm. The blue, orange,

Optics EXPRESS

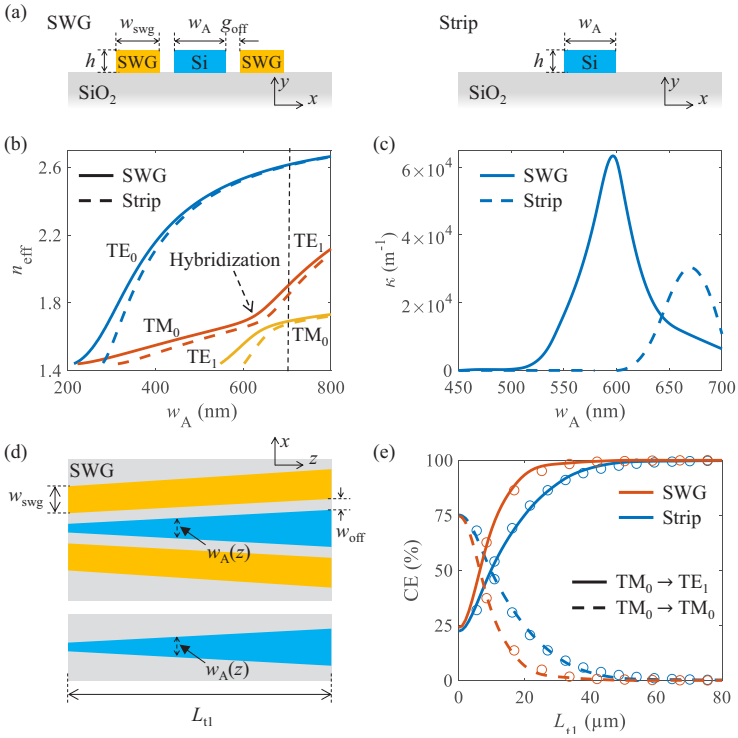

Fig. 2. (a) Schematic cross-sections of the SWG-clad (left) and strip (right) waveguides. (b) Numerically simulated effective refractive indices n_{eff} of SWG-clad (solid lines) and strip (dashed lines): TE_0 (blue), $TM_0 \rightarrow TE_1$ (orange), and $TE_1 \rightarrow TM_0$ (yellow). The black dashed line indicates where w_A=700 nm. (c) Calculated local coupling coefficient κ between TM_0 and TE_1 modes using Eq. (2): SWG-clad (solid) and strip (dashed) waveguides. (d) Top view of the rotation section along the linear taper length L_{t1}: SWG-clad (upper) and strip (lower) waveguides. (e) Simulated mode conversion efficiencies (*CE*s) when TM_0 mode is launched: SWG (orange) and strip (blue). Solid and dashed lines show TM_0 to TE_1 and TM_0 to TM_0 conversions, respectively. Geometric parameters are set to h=220 nm, w_{swg}=250 nm, and g_{off}=50 nm.

and yellow represent TE_{0A}, $TE_{0B} \rightarrow TE_{1A}$, and $TE_{1A} \rightarrow TE_{0B}$ modal indices, respectively. As in the rotation section, the TE_{0A} mode does not experience any modal conversion due to the large effective index difference. However, for the TE_{1A} and TE_{0B} modes, the mode hybridization is shown near $w_B \approx$350 nm with an avoided mode crossing. This hybridization helps the TE_{1A} mode be coupled to TE_{0B}, following the trajectory of the yellow line in Fig. 3(b). This coupling between the TE_{1A} and TE_{0B} modes is more evident in the local coupling coefficient calculations shown in Fig. 3(c). Similar to Fig. 2(c), Eq. (2) was used for this calculation but between TE_{1A} and TE_{0B} modes. Notice the stronger κ with the SWG than the strip configuration. The SWG introduces a large coupling coefficient, facilitating the modal conversion; thus, a shorter conversion length is expected for the SWG-clad waveguides. To confirm this, we conducted the EME simulations for the mode splitting with adiabatically tapered coupled SWG-clad and strip waveguides. From the modal simulations in Fig. 3(b), we chose the w_B=150–500 nm for our tapering width and linearly tapered along the L_{t2} to ensure the conversion. Figures 3(d) and 3(e) show the top views of the linearly tapered mode splitting sections with SWG-clad and strip waveguides, respectively. Figures 3(f) and 3(g) show the mode *CE*s of TE_{1A} to TE_{0B} (solid lines) and TE_{1A} to TE_{1A}

Optics EXPRESS

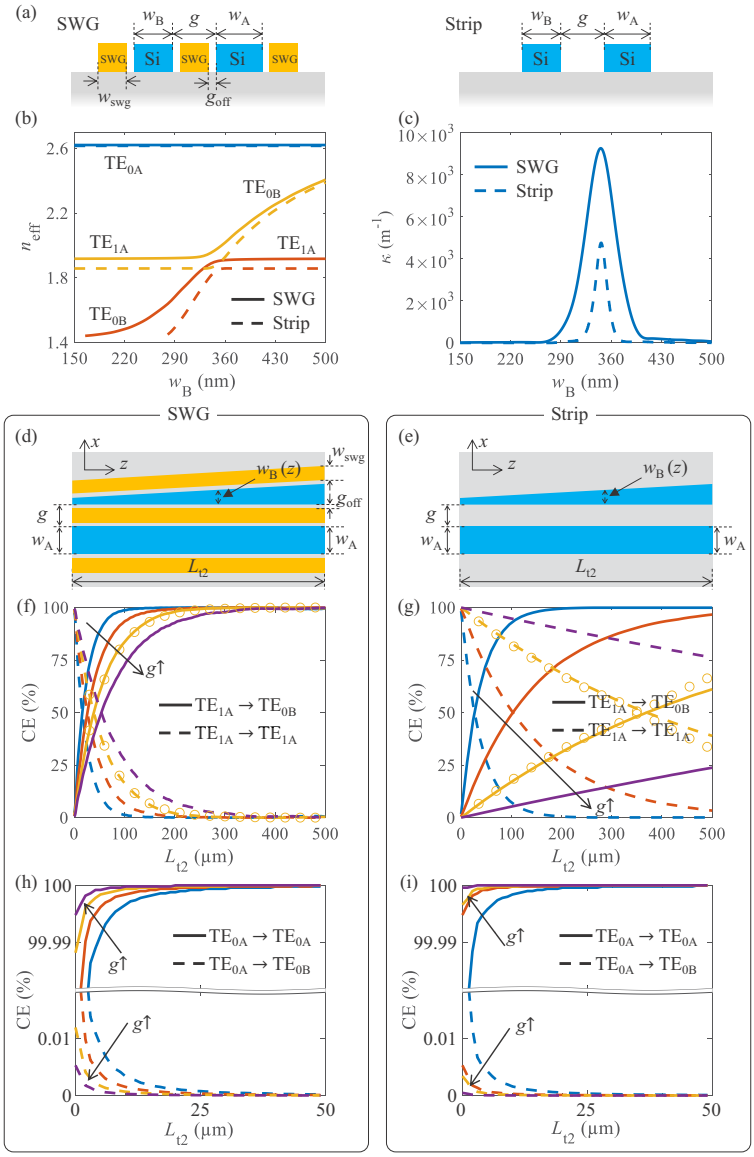

Fig. 3. (a) Schematic cross-sections of the mode splitting section: coupled SWG-clad (left) and strip (right) waveguides. (b) Simulated n_{eff} of SWG-clad (solid lines) and strip (dashed lines) waveguides: TE_{0A} (blue), $TE_{0B} \rightarrow TE_{1A}$ (orange), and $TE_{1A} \rightarrow TE_{0B}$ (yellow). (c) Calculated local coupling coefficient between TE_{1A} and TE_{0B} using Eq. (2): coupled SWG-clad (solid) and strip (dashed) waveguides. Top views of the splitting section with coupled (d) SWG-clad and (e) strip waveguides, where w_A=700 nm and w_B=150–500 nm. Simulated conversion efficiencies (*CE*s) as a function of the taper length L_{t2} for the (f,g) TE_{1A} and (h,i) TE_{0A} inputs: coupled (f,h) SWG-clad and (g,i) strip waveguides. Different colors represent gap sizes: g=150 nm (blue), 250 nm (orange), 350 nm (yellow), and 450 nm (purple), and other parameters are h=220 nm and g_{off}=50 nm.

Optics EXPRESS

(dashed lines) transitions as a function of the taper length L_{t2} for the coupled SWG-clad and strip waveguides, respectively. The yellow circles represent the calculated *CE* results from the local coupled-mode theory using the coefficients in Fig. 3(c), again, confirming the EME results. Different colors represent different gaps g=150 (blue), 250 (orange), 350 (yellow), and 450 nm (purple) while fixing g_{off}=50 nm. Other parameters are the same as in Fig. 1. In both SWG-clad and strip cases, a higher *CE* between TE_{1A} and TE_{0B} is shown for a narrower gap g, obviously due to a stronger coupling. For the strip case [Fig. 3(g)], extensively long coupling length is required, which is the typical limitation of mode-evolution-based adiabatic transition. However, with the SWGs, the coupling length can be shortened due to a stronger coupling [Fig. 3(c)], as shown in Fig. 3(f). To ensure that the TE_{0A} input stays in the same waveguide-A, TE_{0A} to TE_{0A} conversion efficiencies are also simulated in Figs. 3(h) and 3(i), respectively, for the SWG-clad and strip cases. It is clearly seen that there are almost negligible couplings, as mentioned, due to the large index differences.

3. 3D FDTD simulation

From the coupled-mode and EME simulations in Section 2, we set the w_{swg}=250 nm and g_{off}=50 nm (thus, the gap is $g=w_{swg}+2g_{off}$=350 nm), then chose the taper lengths as L_{t1}=50 μm and L_{t2}=250 μm (thus, the total device length is $L=L_{t1}+L_{t2}$=300 μm). These taper lengths are selected to be sufficiently long enough to achieve conversion efficiencies close to 100% [from Figs. 2(e) and 3(f)]. Then, to examine the spectral performance of the designed SWG-PSR, we ran the three-dimensional (3D) finite-difference time-domain (FDTD) simulations for the optimized parameters above. The other parameters are the same as in Fig. 1. Figures 4(a) and 4(b) show the top views of the simulated mode field profiles ($|E|$) while exciting the TE_0 and TM_0 modes at the input (left side), respectively. The free space wavelength is at λ_0=1550 nm. The mode profiles clearly show that the TM_0 input is converted to the TE_1 through the first tapering, then the TE_1

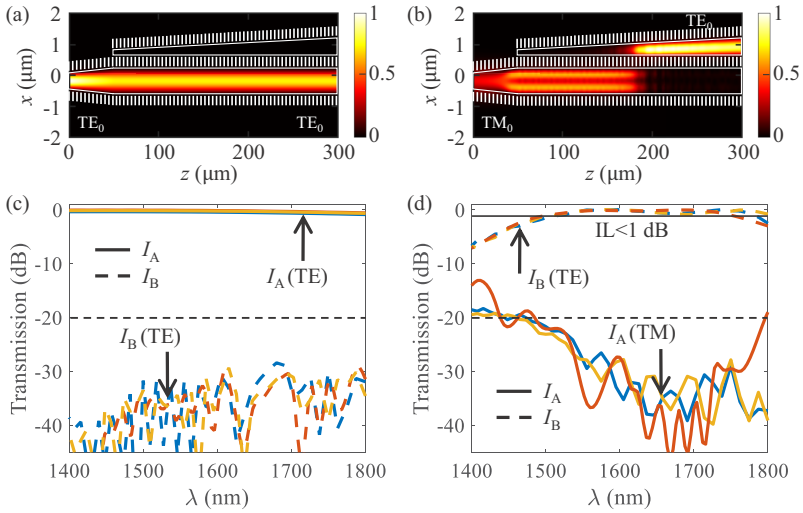

Fig. 4. Full 3D FDTD simulation. (a,b) Top views of the simulated mode field profiles ($|E|$) along the designed SWG-PSR at λ=1550 nm: (a) TE_0 (b) TM_0 inputs. (c,d) Numerically simulated transmission spectra at the output ports of the waveguides-A (I_A, solid) and B (I_B, dashed) while varying SWG filling fraction ρ = 0.45 (blue), 0.5 (orange), and 0.55 (yellow): (c) TE_0 and (d) TM_0 inputs. The taper lengths are set to L_{t1}=50 μm and L_{t2}=250 μm. Other parameters are the same as in Fig. 1. The solid black line shows the IL <1 dB. The black dashed line is a guide to −20 dB transmission.

Optics EXPRESS

is cross-coupled to the TE_0 mode in the waveguide-B [Fig. 4(b)]. For the TE_0 input, it passes through the waveguide-A without coupling to the waveguide-B nor converting to other modes [Fig. 4(a)]. In this way, TE_0 and TM_0 modes are separated while the TM_0 mode is converted to the TE_0 mode at the waveguide-B; thus, only one polarization status exists at the outputs while sorting out the different polarization inputs. Figures 4(c) and 4(d) show the corresponding spectral transmissions for the TE_0 and TM_0 inputs, respectively. The solid and dashed lines represent the output powers at the waveguide-A (I_A) and B (I_B), respectively. Different colors represent different filling fractions of SWG: $\rho = 0.45$ (blue), 0.5 (orange), and 0.55 (yellow). Due to the adiabatic nature of the design, a broadband polarization split-rotation is shown, having >250 nm (1500–1750 nm) bandwidth for the extinction ratio of ER >20 dB and the insertion loss of IL<1 dB. This is difficult to achieve with a traditional strip waveguide-based PSR because it would necessitate extremely long taper lengths, as shown in Fig. 3(g), which may cause additional issues such as scattering losses and fabrication non-uniformity. In addition, the variations in SWG filling fractions $\rho = 0.50 \pm 0.05$ do not affect on the device's performance much, suggesting its fabrication tolerance within ±5 nm. Even though the fabrication imperfections may alter the modal properties in each cross-section, the smooth modal transition characteristics, as shown in Figs. 2(b) and 3(b), still hold, making SWG-PSR very robust to fabrication errors.

4. Experiment

After confirming its spectral results in Section 3, we fabricated and characterized the devices. The devices were fabricated on an SOI wafer consisting of a 220 nm thick Si layer on top of a 2 μm thick silicon dioxide (SiO_2) layer. The electron-beam lithography was used to fabricate the devices [48]. For the characterization, two sets of devices were fabricated for the same PSR design: one with TE input grating coupler and the other with TM input grating coupler. For the output ports of TE excitation, TE grating couplers are employed for ports A and B; and, for the output ports of TM excitation, TM and TE grating couplers are employed for ports A and B, respectively, so that correctly quantify the residual signals. Figure 5(a) shows the microscopic image of the fabricated device layout, where I_{in}, I_A, and I_B denote the optical powers at the input, waveguide-A, and waveguide-B, respectively. Bottom zoomed-in views show (right) tapered waveguide-A for rotation, (middle) asymmetric coupler consisting of waveguide-A and waveguide-B for splitting, and (left) adiabatic transition from the SWG-cladded waveguides to strip waveguides. The red and yellow arrows indicate the guided paths of TE_0 and TM_0 inputs, respectively. We used a custom-built grating coupler stage to measure the spectrum transmissions. Fiber arrays were used to couple in and out a tunable laser source to the chip, and a polarization controller after the laser source regulated the input polarization state. The output light signals were then sent to the photodetectors via other ports of the same fiber array. Figures 5(b) and 5(c) show the characterized transmission spectra of TE_0 (blue) and TM_0 (orange) inputs, respectively. Each spectrum is normalized by the corresponding reference grating coupler spectra. The solid and dashed lines represent the transmissions at waveguide-A (I_A) and B (I_B) outputs, respectively. Similar to the FDTD results in Fig. 4(c), the TE_0 input passes through waveguide-A with a negligible coupling to waveguide-B [Fig. 5(b)], while the TM_0 input is rotated and cross-coupled to the TE_0 mode in the waveguide-B [Fig. 5(c)]. The 20 dB bandwidth of PSR is observed over 1490–1590 nm (>100 nm), which corresponds to the FDTD results in Figs. 4(c) and 4(d) but limited by the laser bandwidth. The ILs are also less than 1.3 dB for the given spectral range. This large bandwidth is due to its adiabatic mode-evolution, while SWGs enhance their conversion strength for a shorter device length. Table 1 summarizes and compares with the previous works on PSRs, and our SWG enhanced PSR is notably competitive compared to other designs balancing the bandwidth and the device length.

Optics EXPRESS

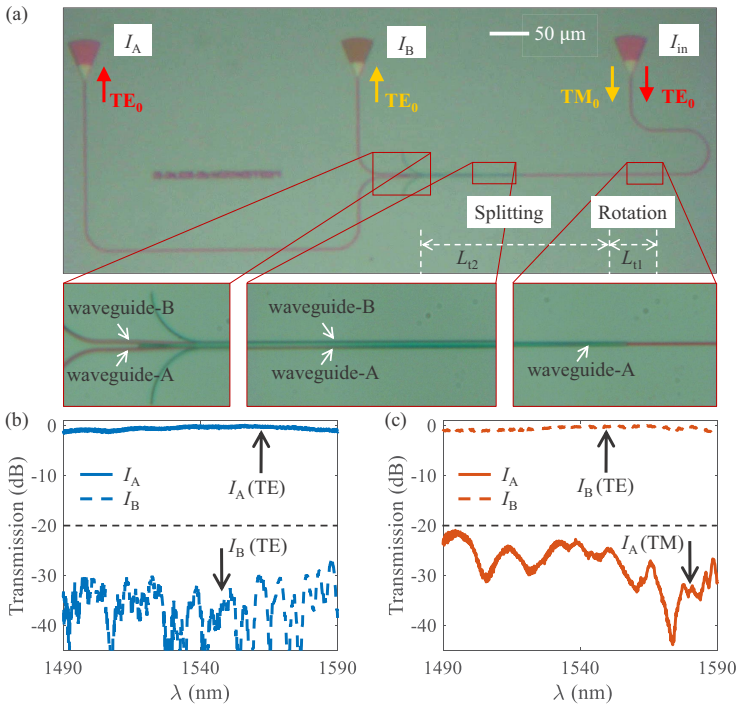

Fig. 5. (a) Microscopic image of the fabricated PSR layout (scale bar=50 μm): I_{in}, I_A, and I_B denote optical powers at the input, output waveguide-A, and output waveguide-B, respectively. Zoomed-in images show (right) tapered waveguide-A, (middle) asymmetric directional coupler (waveguide-A and waveguide-B), and (left) adiabatic transition from the SWG-clad to strip waveguides. (b,c) Experimentally measured transmission spectra at the output waveguides-A (solid) and waveguide-B (dashed): (b) TE_0 (blue) and (c) TM_0 (orange) inputs. The geometric parameters are the same as in Fig. 4. The black dashed line is a guide to −20 dB transmission.

Table 1. Summary of the experimentally demonstrated ER>20 dB photonic PSRs[a]

Structure	BW_{20dB} (nm)	IL (dB)	L (μm)	Mechanism	Clad./Etching
Ridge DC [12]	30	0.5	27	Mode-coupling	SiO_2/Double
Discretized SWG [13]	41	1	7.92	Mode-coupling	Air/Single
Bent DC [14]	70	1	8.77	Mode-coupling	Air/Single
Bent ridge DC [15]	80	3	70	Mode-coupling	SiO_2/Double
Taper+ADC+MMI [28]	50	1.5	70	Hybrid	Air/Single
MMW+ADC+BDC [29]	85	0.57	47.5	Hybrid	Air/Single
Taper+ADC [19]	80	1.6	475	Mode-evolution	SiO_2/Double
Taper+counter ADC [20]	80	0.73	313.5	Mode-evolution	SiO_2/Double
Taper+SWG ADC [21]	80	1.4	171	Mode-evolution	Air/Single
Tapered DC [22]	85	1.5	375	Mode-evolution	SiO_2/Double
This Work Sim.(Exp.)	**250(100[b])**	**1.3**	**300**	**Mode-evolution**	**Air/Single**

[a]BW_{20dB} (bandwidth for ER>20 dB); IL (Insertion loss); L (device length); DC (directional coupler); ADC (Asymmetric directional coupler); MMI (Multimode interferometer); MMW (Multimode waveguide); BDC (Bent DC); Sim. (Simulation); Exp. (Experiment).
[b]Measurement is limited by the laser source bandwidth.

Optics EXPRESS

5. Conclusion

In summary, we proposed a broadband silicon photonic PSR, whose conversion strengths were enhanced by SWGs. Both rotation and splitting sections are designed based on adiabatic modal transitions, providing broad bandwidth, but the conversion lengths are shortened in support of SWGs. The enhanced coupling coefficients in our PSR explicitly show the role of SWGs, which are further confirmed by both local coupled-mode theory and EME simulations. Full 3D FDTD simulations show our PSR can operate over the 1500–1750 nm range (BW_{20dB} >250 nm), and we experimentally report BW_{20dB} >100 nm PSR with a 300 μm long total device length. Our PSR is based on a mode evolution; thus, a high tolerance for fabrication imperfection is expected. One can also increase the gap between the coupled waveguides for a higher extinction ratio but in the trade of a longer device length. The total device length also could be further shortened by optimizing the tapering widths [55]. Our PSR is designed on an SOI platform and immediately applicable to a broad range of silicon photonic systems, such as on-chip coherent optical communications and wavelength division multiplexing.

Funding. National Science Foundation (1930784, 2144568); U.S. Department of Energy (DE-NA-0003525); Korea Advanced Institute of Science and Technology (G04220043).

Acknowledgments. This work was performed, in part, at the Center for Integrated Nanotechnologies (CINT), an Office of Science User Facility operated for the U.S. Department of Energy Office of Science by Los Alamos National Laboratory and Sandia National Laboratories. S. K. acknowledges the support from the KSEA young investigator grant.

Disclosures. The authors declare no conflicts of interest regarding this article.

Data availability. Upon reasonable request, the corresponding author will provide data and code supporting the results presented in this paper

References

1. S. Kim and M. Qi, "Copper nanorod array assisted silicon waveguide polarization beam splitter," Opt. Express **22**(8), 9508–9516 (2014).
2. H. Xu, D. Dai, and Y. Shi, "Ultra-broadband and ultra-compact on-chip silicon polarization beam splitter by using hetero-anisotropic metamaterials," Laser Photonics Rev. **13**(4), 1800349 (2019).
3. C. Li, M. Zhang, J. E. Bowers, and D. Dai, "Ultra-broadband polarization beam splitter with silicon subwavelength-grating waveguides," Opt. Lett. **45**(8), 2259–2262 (2020).
4. M. Mia, S. Z. Ahmed, N. Jaidye, I. Ahmed, and S. Kim, "Mode-evolution-based ultra-broadband polarization beam splitter using adiabatically tapered extreme skin-depth waveguide," Opt. Lett. **46**(18), 4490–4493 (2021).
5. S. Z. Ahmed, I. Ahmed, M. Mia, N. Jaidye, and S. Kim, "Ultra-high extinction ratio polarization beam splitter with extreme skin-depth waveguide," Opt. Lett. **46**(9), 2164–2167 (2021).
6. L. Liu, Q. Deng, and Z. Zhou, "Manipulation of beat length and wavelength dependence of a polarization beam splitter using a subwavelength grating," Opt. Lett. **41**(21), 5126–5129 (2016).
7. A. Herrero-Bermello, A. Dias-Ponte, J. M. Luque-González, A. Ortega-Mo nux, A. V. Velasco, P. Cheben, and R. Halir, "Experimental demonstration of metamaterial anisotropy engineering for broadband on-chip polarization beam splitting," Opt. Express **28**(11), 16385–16393 (2020).
8. X. Guan, P. Chen, S. Chen, P. Xu, Y. Shi, and D. Dai, "Low-loss ultracompact transverse-magnetic-pass polarizer with a silicon subwavelength grating waveguide," Opt. Lett. **39**(15), 4514–4517 (2014).
9. B. Bai, L. Liu, R. Chen, and Z. Zhou, "Low loss, compact tm-pass polarizer based on hybrid plasmonic grating," IEEE Photonics Technol. Lett. **29**(7), 607–610 (2017).
10. H. Xu, D. Dai, and Y. Shi, "Anisotropic metamaterial-assisted all-silicon polarizer with 415-nm bandwidth," Photonics Res. **7**(12), 1432–1439 (2019).
11. Z. Lin, X. Li, and S. He, "High-performance silicon te-pass polarizer assisted by anisotropic metamaterials," Opt. Express **30**(14), 24841–24851 (2022).
12. H. Guan, A. Novack, M. Streshinsky, R. Shi, Q. Fang, A. E.-J. Lim, G.-Q. Lo, T. Baehr-Jones, and M. Hochberg, "Cmos-compatible highly efficient polarization splitter and rotator based on a double-etched directional coupler," Opt. Express **22**(3), 2489–2496 (2014).
13. Y. Liu, S. Wang, Y. Wang, W. Liu, H. Xie, Y. Yao, Q. Song, X. Zhang, Y. Yu, and K. Xu, "Subwavelength polarization splitter–rotator with ultra-compact footprint," Opt. Lett. **44**(18), 4495–4498 (2019).
14. Y. Zhang, Y. He, X. Jiang, B. Liu, C. Qiu, Y. Su, and R. A. Soref, "Ultra-compact and highly efficient silicon polarization splitter and rotator," APL Photonics **1**(9), 091304 (2016).
15. K. Tan, Y. Huang, G.-Q. Lo, C. Yu, and C. Lee, "Experimental realization of an o-band compact polarization splitter and rotator," Opt. Express **25**(4), 3234–3241 (2017).

Optics EXPRESS

16. Y. Xiong, J. G. Wangüemert-Pérez, D.-X. Xu, J. H. Schmid, P. Cheben, and N. Y. Winnie, "Polarization splitter and rotator with subwavelength grating for enhanced fabrication tolerance," Opt. Lett. **39**(24), 6931–6934 (2014).
17. Y. Wang, M. Ma, H. Yun, Z. Lu, X. Wang, N. A. Jaeger, and L. Chrostowski, "Ultra-compact sub-wavelength grating polarization splitter-rotator for silicon-on-insulator platform," IEEE Photonics J. **8**(6), 1–9 (2016).
18. Y. R. Bustamante, G. B. de Farias, H. A. de Andrade, and H. E. Hernandez-Figueroa, "Demonstration of a silicon polarization splitter and rotator based on a bow-tie structure," Photonics Nanostruct. **45**, 100921 (2021).
19. W. D. Sacher, T. Barwicz, B. J. Taylor, and J. K. Poon, "Polarization rotator-splitters in standard active silicon photonics platforms," Opt. Express **22**(4), 3777–3786 (2014).
20. Y. Zhao, C. Qiu, A. Wu, H. Huang, J. Li, Z. Sheng, W. Li, X. Wang, and F. Gan, "Broadband polarization splitter-rotator and the application in wdm receiver," IEEE Photonics J. **11**(1), 1–10 (2019).
21. M. Ma, A. H. Park, Y. Wang, H. Shoman, F. Zhang, N. A. Jaeger, and L. Chrostowski, "Sub-wavelength grating-assisted polarization splitter-rotators for silicon-on-insulator platforms," Opt. Express **27**(13), 17581–17591 (2019).
22. A. Melikyan and P. Dong, "Adiabatic mode converters for silicon photonics: Power and polarization broadband manipulators," APL Photonics **4**(3), 030803 (2019).
23. C. Sun, Y. Yu, G. Chen, and X. Zhang, "A low crosstalk and broadband polarization rotator and splitter based on adiabatic couplers," IEEE Photonics Technol. Lett. **28**(20), 2253–2256 (2016).
24. Y. Xiong, D.-X. Xu, J. H. Schmid, P. Cheben, S. Janz, and N. Y. Winnie, "Fabrication tolerant and broadband polarization splitter and rotator based on a taper-etched directional coupler," Opt. Express **22**(14), 17458–17465 (2014).
25. X. Tu, M. Li, J. Xing, H. Fu, and D. Geng, "Compact psr based on an asymmetric bi-level lateral taper in an adiabatic directional coupler," J. Lightwave Technol. **34**(3), 985–991 (2016).
26. Y. Yin, Z. Li, and D. Dai, "Ultra-broadband polarization splitter-rotator based on the mode evolution in a dual-core adiabatic taper," J. Lightwave Technol. **35**(11), 2227–2233 (2017).
27. H.-C. Chung, G.-X. Lu, and S.-Y. Tseng, "Shortcut to adiabaticity in a silicon polarization splitter rotator using multi-wavelength adiabaticity engineering," Opt. Express **30**(5), 8115–8125 (2022).
28. D. Dai and H. Wu, "Realization of a compact polarization splitter-rotator on silicon," Opt. Lett. **41**(10), 2346–2349 (2016).
29. H. Xu and Y. Shi, "Ultra-broadband silicon polarization splitter-rotator based on the multi-mode waveguide," Opt. Express **25**(15), 18485–18491 (2017).
30. Y. Ding, H. Ou, and C. Peucheret, "Wideband polarization splitter and rotator with large fabrication tolerance and simple fabrication process," Opt. Lett. **38**(8), 1227–1229 (2013).
31. T. Barwicz, M. R. Watts, M. A. Popović, P. T. Rakich, L. Socci, F. X. Kärtner, E. P. Ippen, and H. I. Smith, "Polarization-transparent microphotonic devices in the strong confinement limit," Nat. Photonics **1**(1), 57–60 (2007).
32. H. Fukuda, K. Yamada, T. Tsuchizawa, T. Watanabe, H. Shinojima, and S.-I. Itabashi, "Silicon photonic circuit with polarization diversity," Opt. Express **16**(7), 4872–4880 (2008).
33. D. Dai, L. Liu, S. Gao, D.-X. Xu, and S. He, "Polarization management for silicon photonic integrated circuits," Laser Photonics Rev. **7**(3), 303–328 (2013).
34. J. Wang, D. Bonneau, M. Villa, J. W. Silverstone, R. Santagati, S. Miki, T. Yamashita, M. Fujiwara, M. Sasaki, H. Terai, M. G. Tanner, C. M. Natarajan, R. H. Hadfield, J. L. O'Brien, and M. G. Thompson, "Chip-to-chip quantum photonic interconnect by path-polarization interconversion," Optica **3**(4), 407–413 (2016).
35. L.-T. Feng, M. Zhang, Z.-Y. Zhou, M. Li, X. Xiong, L. Yu, B.-S. Shi, G.-P. Guo, D.-X. Dai, X.-F. Ren, and G.-C. Guo, "On-chip coherent conversion of photonic quantum entanglement between different degrees of freedom," Nat. Commun. **7**(1), 11985 (2016).
36. T. Pfau, R. Peveling, J. Hauden, N. Grossard, H. Porte, Y. Achiam, S. Hoffmann, S. K. Ibrahim, O. Adamczyk, S. Bhandare, D. Sandel, M. Porrmann, and R. Noé, "Coherent digital polarization diversity receiver for real-time polarization-multiplexed qpsk transmission at 2.8 Gb/s," IEEE Photonics Technol. Lett. **19**(24), 1988–1990 (2007).
37. P. Dong, X. Liu, S. Chandrasekhar, L. L. Buhl, R. Aroca, and Y.-K. Chen, "Monolithic silicon photonic integrated circuits for compact 100^{+} Gb/s coherent optical receivers and transmitters," IEEE J. Sel. Top. Quantum Electron. **20**(4), 150–157 (2014).
38. H. Zhou, Y. Zhao, Y. Wei, F. Li, J. Dong, and X. Zhang, "All-in-one silicon photonic polarization processor," Nanophotonics **8**(12), 2257–2267 (2019).
39. P. Cheben, R. Halir, J. H. Schmid, H. A. Atwater, and D. R. Smith, "Subwavelength integrated photonics," Nature **560**(7720), 565–572 (2018).
40. R. Halir, A. Ortega-Monux, D. Benedikovic, G. Z. Mashanovich, J. G. Wangüemert-Pérez, J. H. Schmid, I. Molina-Fernandez, and P. Cheben, "Subwavelength-grating metamaterial structures for silicon photonic devices," Proc. IEEE **106**(12), 2144–2157 (2018).
41. J. M. Luque-González, A. Sánchez-Postigo, A. Hadij-ElHouati, A. Ortega-Mo nux, J. G. Wangüemert-Pérez, J. H. Schmid, P. Cheben, Í. Molina-Fernández, and R. Halir, "A review of silicon subwavelength gratings: building break-through devices with anisotropic metamaterials," Nanophotonics (2021).
42. N. Kazanskiy, M. Butt, and S. Khonina, "Silicon photonic devices realized on refractive index engineered subwavelength grating waveguides-a review," Opt. Laser Technol. **138**, 106863 (2021).
43. C. Li, M. Zhang, H. Xu, Y. Tan, Y. Shi, and D. Dai, "Subwavelength silicon photonics for on-chip mode-manipulation," PhotoniX **2**(1), 11–35 (2021).

Optics EXPRESS

44. Z. Guo, J. Xiao, and S. Wu, "Ultracompact, polarization-independent, and highly scalable optical power splitting model employing fan-out bending metamaterials," Photonics Res. **10**(11), 2448–2459 (2022).
45. S. Jahani and Z. Jacob, "Transparent subdiffraction optics: nanoscale light confinement without metal," Optica **1**(2), 96–100 (2014).
46. J. M. Luque-González, A. Herrero-Bermello, A. Ortega-Mo nux, Í. Molina-Fernández, A. V. Velasco, P. Cheben, J. H. Schmid, S. Wang, and R. Halir, "Tilted subwavelength gratings: controlling anisotropy in metamaterial nanophotonic waveguides," Opt. Lett. **43**(19), 4691–4694 (2018).
47. S. Jahani, S. Kim, J. Atkinson, J. C. Wirth, F. Kalhor, A. A. Noman, W. D. Newman, P. Shekhar, K. Han, V. Van, R. G. DeCorby, L. Chrostowski, M. Qi, and Z. Jacob, "Controlling evanescent waves using silicon photonic all-dielectric metamaterials for dense integration," Nat. Commun. **9**(1), 1893 (2018).
48. M. Mia, S. Z. Ahmed, I. Ahmed, Y. J. Lee, M. Qi, and S. Kim, "Exceptional coupling in photonic anisotropic metamaterials for extremely low waveguide crosstalk," Optica **7**(8), 881–887 (2020).
49. M. Kabir, M. Mia, I. Ahmed, N. Jaidye, S. Z. Ahmed, and S. Kim, "Anisotropic subwavelength grating perturbation enables zero crosstalk in a leaky mode," *arXiv*, arXiv:2210.08741 (2022).
50. L. Liu, Y. Ding, K. Yvind, and J. M. Hvam, "Efficient and compact te–tm polarization converter built on silicon-on-insulator platform with a simple fabrication process," Opt. Lett. **36**(7), 1059–1061 (2011).
51. J. Chen and J. Xiao, "Ultracompact silicon-based polarization splitter and rotator based on asymmetric directional couplers with subwavelength gratings," J. Opt. Soc. Am. B **39**(1), 345–354 (2022).
52. G. W. Milton, *The theory of composites* (Cambridge University Press, 2002).
53. J. Mu and W.-P. Huang, "Complex coupled-mode theory for tapered optical waveguides," Opt. Lett. **36**(6), 1026–1028 (2011).
54. S. Chen, Y.-g. Liu, Z. Wang, H. Guo, H. Zhang, and B. Mao, "Mode transmission analysis method for photonic lantern based on FEM and local coupled mode theory," Opt. Express **28**(21), 30489–30501 (2020).
55. S. Kim and M. Qi, "Mode-evolution-based polarization rotation and coupling between silicon and hybrid plasmonic waveguides," Sci. Rep. **5**(1), 18378 (2015).